

A Magnetically-Actuated Untethered Jellyfish-Inspired Soft Milliswimmer

Ziyu Ren^{1*}, Tianlu Wang^{1*}, Wenqi Hu¹, Metin Sitti^{1#}

Abstract— Untethered small-scale soft robots can potentially be used in healthcare and biomedical applications. They can access small spaces and reshape their bodies in a programmable manner to adapt to unstructured environments and have diverse dynamic behaviors. However, the functionalities of current miniature soft robots are limited, restricting their applications in medical procedures. Taking the advantage of the shape-programmable ability of magnetic soft composite materials, here we propose an untethered soft millirobot (jellyfishbot) that can swim like a jellyfish by time- and trajectory-asymmetric up and down beating of its lappets. Its swimming speed and direction can be controlled by tuning the magnitude, frequency, and direction of the external oscillating magnetic field. We demonstrate that such jellyfishbot can perform several tasks that could be useful towards medical applications, such as delivering drugs, clogging a narrow tube or vessel, and patching a target area under ultrasound imaging-based guiding. The millirobot presented in this paper could be used inside organs filled with fluids completely, such as a bladder or inflated stomach.

Keywords– Bio-inspired; soft robot; miniature robot; jellyfish

I. INTRODUCTION

Miniature robots with sizes ranging from tens of micrometers up to several centimeters [1] have significant potential on environmental exploration and remediation [2][3], surveillance [4], and healthcare applications [1], [5]. Specifically, untethered medical miniature robots could access to delicate and narrow regions of the human body, such as inside the eye, brain, bladder, blood vessels/capillaries, and gastrointestinal tract. They can provide minimally invasive disease diagnosis and treatment [1], [5]–[10]. In contrast to existing rigid-body miniature robots [5], [11], soft miniature robots are shape-programmable with very high degrees of freedom and can adapt to environmental constraints physically [12], [13]. They have greater potential to realize high mobility and achieve multiple functionalities towards biomedical applications. Among various active soft materials to create untethered soft miniature robots [14]–[20], magnetic soft composite materials are promising for medical applications [13], [21], [22] due to three reasons. First, high magnetic fields used as the actuation input can safely penetrate the human body without damaging living tissues [23], [24]. Next, magnetic fields can be specified not only in magnitude but also in 3D direction and spatial gradient, which provides a large actuation

control space [21]. Last, the magnetization profile of magnetic soft composite materials can be programmed flexibly, which can be exploited to achieve complex and high-spatial-resolution shape deformations [21].

In previous studies, magnetic soft composite materials have been applied to achieve high-performance locomotion in different working conditions, such as swimming on the water surface [25] or within the viscous fluid [12], moving across the wet slippery area [26], and negotiating unstructured environments with multiple locomotion modes [13]. Apart from the locomotion performance, some of these robots also demonstrate their functionalities towards medical uses. The robot presented in [26] can carry a capsule that is much heavier than its body weight. However, the capsule is stuck to the robot body and cannot be released at the desired position. The robot developed in [13] shows preliminary results of soft robotic basic pick-and-place and cargo-release functions. Up to now, the functionalities of soft miniature robots are still limited, restricting their use in medical applications. Further enhancing the functionalities of small-scale soft robots has not been resolved yet.

In this paper, we propose a jellyfish-inspired soft millirobot made of magnetic soft composite materials towards achieving multiple medical tasks. As one of the most successful and widely-spread oceanic creatures around the world [27], jellyfish ephyra possesses a body size ranging from several millimeters to one centimeter and adopts paddling motion for both swimming and predation in moderate Reynolds numbers [28], [29]. The ephyra jellyfish provides an ideal paradigm to small-scale swimming robots that have similar characteristic length scale and work in similar fluid environments. We experimentally demonstrate that the robot inspired by jellyfish can achieve several medical tasks, including delivering cargo, clogging the narrow tube, and patching the target through ultrasound guiding. These functionalities could enable the robot to be applied to a treatment process inside organs filled with a fluid, such as a bladder and inflated stomach.

II. DESIGN AND FABRICATION

The design parameters of the robot can be found in Fig. 1a-i. The robot body is composed of two parts: the active part that works like muscles to achieve the paddling motion, and the passive part that fills the gaps of the active part, making the body into a continuous hydrodynamic surface. The active part of the body is made of soft magnetic material that can deform under external \mathbf{B} field. Following the fabrication procedure presented in Hu et al. [13], we prepare the material by mixing

¹Physical Intelligence Department, Max Planck Institute for Intelligent Systems, 70569 Stuttgart, Germany. *Equally contributing authors. #Correspondence to: sitti@is.mpg.de

the neodymium-iron-boron (NdFeB) magnetic microparticles (MQP-15-7, Magnequench; average diameter: 5 μm) with the polymer (Ecoflex 00-10, Smooth-On Inc.) by a mass ratio of 1:1. The mixture is cast onto a poly(methyl-methacrylate) (PMMA) plate coated with parylene-C. The polymer is cured at 60°C to form a thin membrane with a thickness of around 96 μm (Fig. 1b-i). The geometry of the active part is cut out from this thin membrane using the laser cutter (Fig. 1b-ii). After moving the active part from the flat plate, a water droplet is dropped on it using a pipette. The active part can immediately wrap the water droplet and form an ellipsoidal shape under the surface tension (Fig. 1b-iii). Then the active part is put into a fridge to be frozen to keep the ellipsoidal shape. The ellipsoidal active part is magnetized by a 1.8 T uniform magnetic field inside a vibrating sample magnetometer (VSM, EZ7, Microsense). After magnetization, the gaps of the active part are filled with a non-magnetic elastomer (Ecoflex 00-10) to form a thin-layer film with a thickness of around 20 μm (Fig. 1b-iv). The snapshot of the final robot is shown in Fig. 1a-ii.

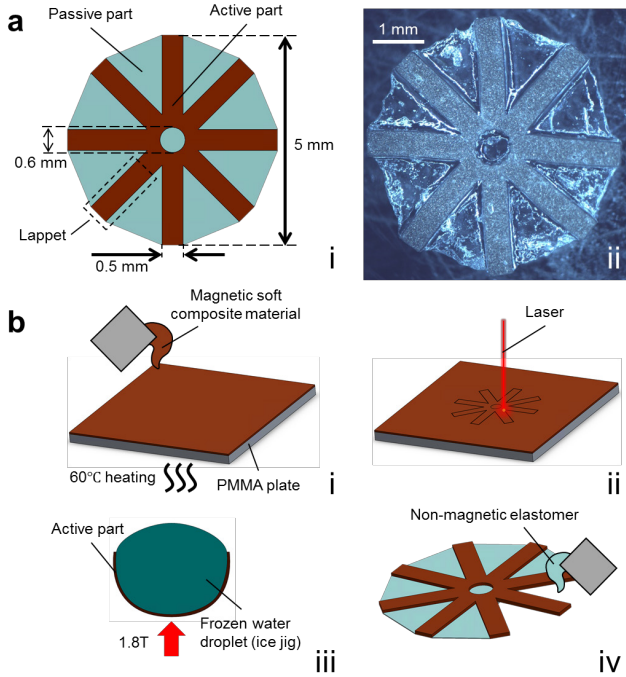


Figure 1. Design and fabrication of the jellyfish-inspired soft millirobot with 8 lappets similar to ephyra: (a) The design parameters of the robot are shown in (i) and the snapshot of the final robot is shown in (ii). (b) The fabrication process steps: (i) The magnetic soft composite material is cast onto a PMMA plate. The material is cured at 60°C to form a thin membrane; (ii) The active part of the robot is cut out from the magnetic soft composite material membrane using the laser cutter; (iii) The active part is shaped into an ellipsoid using a frozen ice jig. It is magnetized by a 1.8 T uniform magnetic field; (iv) The gaps of the active part are filled with a non-magnetic elastomer.

III. MAGNETIC ACTUATION AND STEERING STRATEGY

All the experiments are conducted in a custom-made electromagnetic coil system, which can provide \mathbf{B} field with magnitude ranging from 0-20 mT, with the global system XYZ

fixed at its center. The body-attached frame ($X'Y'Z'$) moving along with the robot is shown in Fig. 2. The robot swims in a transparent water tank put at the center of the working space. The deformation of the robot depends on the magnitude of the external \mathbf{B} field. When applying a constant \mathbf{B} field along Y' direction, the robot can bend either upwards ($B_{Y'} > 0$) or downwards ($B_{Y'} < 0$). The bending amplitude can be tuned by adjusting the magnitude of the \mathbf{B} field (Fig. 2). However, the experiments also show that there exists a saturation magnitude, which is around 10 mT, so that the deformation of the body doesn't increase with an even larger \mathbf{B} field. If we apply a \mathbf{B} field oscillating along Y' axis (for example, by applying the waveforms shown in Fig. 4a), the robot can continuously beat up and down, realizing the paddling motion inspired by a real jellyfish [29]. Since the net magnetic moment of the robot is always aligned with its body central axis, i.e., the Y' direction of the body-attached frame (the red coordinate system plotted in Fig. 2), the robot always tends to align its body central axis to the direction of the external \mathbf{B} field. Therefore, the robot can be steered by simply changing the oscillating axis of the external \mathbf{B} field.

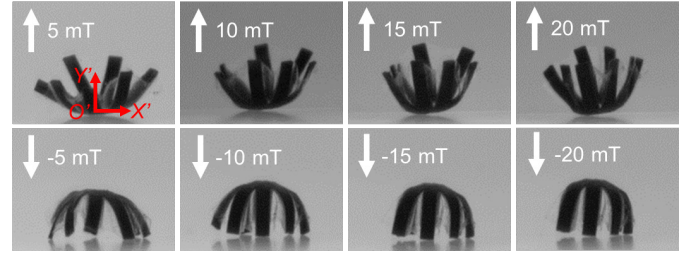


Figure 2. Deformation of the robot under constant \mathbf{B} fields with different magnitudes. The body-attached frame is plotted in red.

IV. MODELING OF THE PROPULSION PERFORMANCE

To better understand the relationship between the robot kinematics and its propulsion performance, a simplified dynamic model is developed in this section.

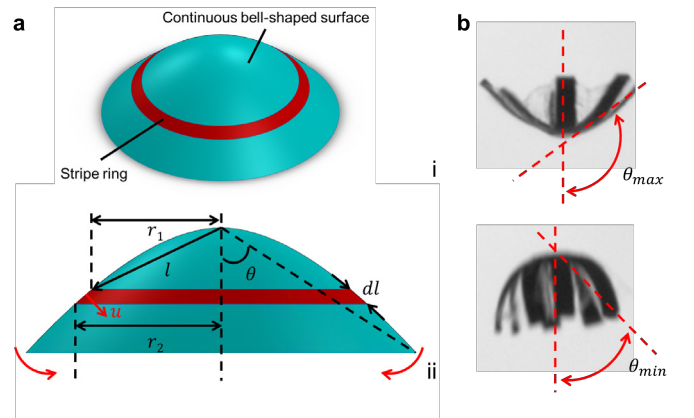


Figure 3. Illustration of the simplified dynamic model. (a) Schematic illustration: (i) The thrust force is estimated by integrating the drag force acting on the stripe ring with infinitesimal width (dl); (ii) The geometry parameters used in the simplified model. (b) The beating angles achieved when the robot lappets deform to extreme positions.

During propulsion, following forces are considered to act on the robot body and cause the changing of the robot acceleration: the thrust force \mathbf{T} produced by the paddling motion, the drag force \mathbf{D} acting on the bell-shaped body, the added mass force \mathbf{A} resulting from accelerating the surrounding fluid, and the gravity force \mathbf{G} . According to Newton's second law, the following equation holds at each time instant:

$$\mathbf{T} - \mathbf{D} - \mathbf{A} - \mathbf{G} = m \frac{d\mathbf{v}}{dt}, \quad (1)$$

where m is the mass of the robot and is measured to be 2.05×10^{-6} kg. \mathbf{v} is the instantaneous velocity of the robot. The drag-based thrust force provided by the paddling motion is estimated with a simple fluid-solid interaction model. The robot body is represented as a bell-shaped surface consisting of many stripe rings with infinitesimal width, which is assumed to move against to the flow with velocity \mathbf{u} (Fig. 3a). The wetted area of each stripe ring is approximated with the lateral surface of a circular truncated cone expressed as:

$$S_{stripe} = \pi(r_1 + r_2)dl. \quad (2)$$

The thrust force \mathbf{T} can be estimated from [30]:

$$\mathbf{T} = \frac{1}{2} C_{stripe} S_{stripe} \rho \mathbf{u} \cos\theta, \quad (3)$$

where θ is the beating angle defined in Fig. 3b, C_{stripe} is the drag coefficient of the stripe ring, which is 1.98 following [30]. ρ is the water density. The drag force \mathbf{D} is calculated as [30]:

$$\mathbf{D} = \frac{1}{2} C_{bell} S_{bell} \rho \mathbf{v} \mathbf{v}, \quad (4)$$

where S_{bell} is the instantaneous projection area of the robot body, and C_{bell} is the drag coefficient. S_{bell} is calculated as:

$$S_{bell} = \pi(L \sin\theta)^2, \quad (5)$$

where $L = 2.5$ mm is the radius of the robot body. We assume the drag acting on the bell-shaped body is close to the drag acting on a sphere translating in flow, and therefore C_{bell} can be estimated using the following equation [31]:

$$c_{bell} = \frac{24}{Re_B} (1 + 0.173 Re_B^{0.657}) + \frac{0.413}{1 + 163000 Re_B^{-1.09}}. \quad (6)$$

The added mass force \mathbf{A} is estimated by assuming the body accelerates along with the water within the hemi-ellipsoid sub-umbrella cavity [30]:

$$\mathbf{A} = \alpha \rho V \frac{d\mathbf{v}}{dt}, \quad (7)$$

where the added mass coefficient α and the sub-umbrella volume V are [30]:

$$\alpha = \tan^{-1.4}\theta \quad (8-1)$$

$$V = \frac{2\pi L^3 \sin^2\theta \cos\theta}{3}. \quad (8-2)$$

The deformation of the robot body is determined by both the internal stress, the magnetic torque and the hydrodynamic force, and is hard to predict. Therefore, θ is directly measured from the high-speed videos. When the robot beats upwards and reaches an extreme position, θ reaches its maximum value,

θ_{max} . When the robot beats downwards and reaches another extreme position, θ reaches its minimum value, θ_{min} (Fig. 3b). According to the change in θ , the motion of the robot in one cycle can be divided into three phases. During the recovery phase, θ changes from θ_{min} to θ_{max} with angular velocity ω_r in time period T_r . During the contraction phase, θ changes from θ_{max} to θ_{min} with angular velocity ω_c in time period T_c . During the glide phase, θ keeps constant in time period T_g . For simplicity, we assume ω_c and ω_r are constant. Therefore, by measuring θ_{max} , θ_{min} , T_c , and T_r , we can determine ω_c and ω_r as:

$$\omega_r = \frac{(\theta_{max} - \theta_{min})}{T_r} \quad (9-1)$$

$$\omega_c = \frac{(\theta_{max} - \theta_{min})}{T_c}. \quad (9-2)$$

The instantaneous velocity of the robot \mathbf{v} is numerically solved using the Runge-Kutta method in Matlab (version 2018a, Mathworks). For each case, \mathbf{v} is calculated for eight complete cycles. The average swimming speed is calculated by integrating the instantaneous velocity of the last five cycles. The results are presented in Fig. 5.

V. CHARACTERIZATION OF PROPULSION PERFORMANCE

We preliminarily investigate the propulsion performance of the robot under control signals with different magnitudes and frequencies. Two waveforms of the control signals are used in this paper and shown as large amplitude and small amplitude signals in Fig. 4a. They only differ in their peak value. In the first characterization experiment, we let the robot swim directly from the tank bottom using these two waveforms with actuation frequency of 10 Hz. The kinematics during one propulsion cycle (Fig. 4b) and the variations of the beating angles within two consecutive cycles (Fig. 4c) are obtained. Compared to the control waveform with a smaller peak value, the control signal with a larger peak value induces a larger beating amplitude and a higher beating angular velocity, resulting in a larger traveling distance per cycle and a higher swimming speed.

To see the influence of the actuation frequency on robot performance, we then increase the actuation frequency of the control signals from 5 Hz to 40 Hz to control the robot to swim straightly upwards from the tank bottom. Each trial is repeated for five times. The variations of the beating amplitude and the average swimming velocity are shown in Fig. 5. From the experiments, we observe that the beating amplitude of the robot monotonically decreases with the increasing frequency (Fig. 5a). This is because the hydrodynamic force from the surrounding fluid works as a damping force that prevents the deformation of the robot body. Since the hydrodynamic force acting on the robot is positively related to the beating velocity, the higher the actuation frequency is applied, the larger the damping force is produced and the smaller the deformation of the robot is obtained. Therefore, when the robot is actuated at high frequency, compensation to the magnitude of the external \mathbf{B} field is required to reach the desired deformation.

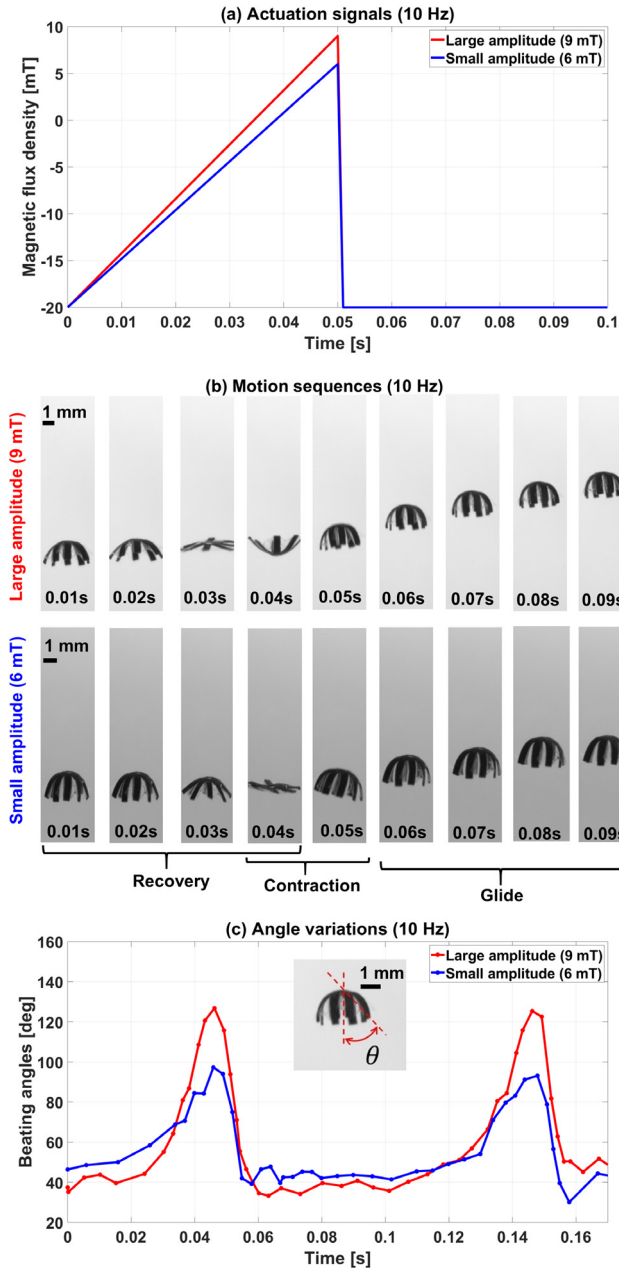


Figure 4. Actuation signals and kinematics of the robot at actuation frequency of 10 Hz. (a) Large and small actuation signals. (b) Motion sequences under these two actuation signals. A complete cycle includes three phases: recovery phase, contraction phase, and glide phase. The kinematics at different actuation signals are shown in Video part 1. (c) Variations of the beating angles of two actuation signals within two cycles.

Although higher actuation frequencies tend to increase the number of beatings within a given period, they decrease the beating amplitude at the same time (because it is harder for the robot to follow actuation signals with higher frequencies). These two factors bring up contradictory influences on the swimming velocity. Both the experiment results and the prediction from the simplified dynamic model suggest that the robot can reach a peak swimming speed at an actuation frequency between 10–20 Hz (Fig. 5b). When the frequency continues to increase, the swimming speed decreases along

with the decrement in beating amplitude. The average swimming speed obtained using smaller amplitude signal drops faster than larger amplitude signal, and even becomes negative at 40 Hz. The investigation on actuation frequency shows that there exists an optimal actuation frequency to a given control signal waveform. A more accurate dynamic model that incorporates the influence of the hydrodynamic force on the material deformation (fluid-structure interaction) would help us find the optimal control scheme in the future.

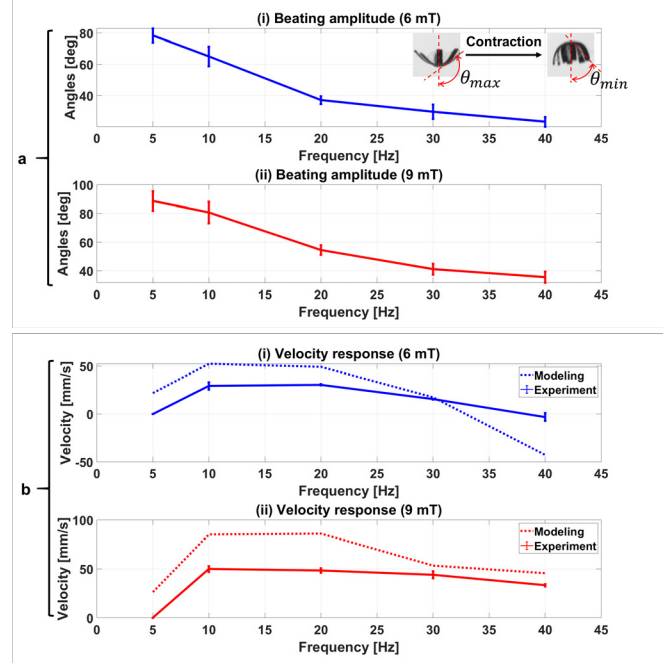


Figure 5. The influence of actuation frequencies on the robot's kinematics and swimming performance. The velocities and kinematics at different actuation frequencies are shown in Video part 1. (a) The variation of the beating amplitude with the increasing actuation frequency. (b) The variation of the swimming speed with the increasing actuation frequency. The error bars represent the standard deviation.

VI. DEMONSTRATION OF FUNCTIONS TOWARDS MEDICAL APPLICATIONS

Untethered miniature robots are anticipated to be able to conduct various clinical medical functions in the future, such as realizing local drug delivery, embolization, and patching cancerous tissues or wounds [1], [9] inside stagnant fluid-filled organs, such as bladder or inflated stomach, and being guided by ultrasound to realize high-precision position control [13]. In this section, we demonstrate preliminary experiments to show that our robot could have the potential to achieve these functions.

First, we demonstrate the robot has the ability to swim across a barrier while carrying a cargo and then releasing the cargo at a desired position. A polystyrene bead (Polysciences, Inc., density: 1.05 g/cc, diameter: 1 mm) is desired to be delivered from right to left separated by an obstacle (5 mm in width and 15 mm in height in Fig. 6). At the beginning, the robot rests on the tank bottom with the polystyrene bead stick to the robot

body within the sub-umbrella region. Then we apply an oscillation \mathbf{B} field with the waveform of small amplitude (the blue profile in Fig. 4a) at a frequency of 15 Hz to let the robot swim close to the obstacle. Since the control signal induces a small body deformation, the bead is firmly attached to the robot body at this stage. When the robot reaches the height of the obstacle, we gradually rotate the oscillating direction of the \mathbf{B} field and steer the robot to bypass the obstacle. After the robot swims away from the obstacle, we suddenly change the orientation of the oscillating axis of the \mathbf{B} field from horizontal to vertical and switch the control waveform from small amplitude to large amplitude (the red profile in Fig. 4a) in order to induce a larger beating amplitude to shake the bead off rapidly. The whole process is shown in Fig. 6 and the first scene of the Video part 2. This demo suggests the potential of the robot to be steered in unstructured environments and realize drug delivery and sampling.

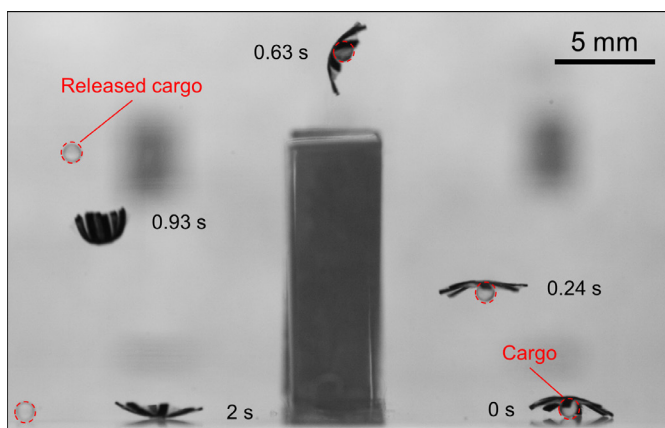


Figure 6. Cargo transport demonstration of the robot: The video snapshots of the robot and the bead are overlaid in the same video image. The red dashed circles indicate the positions of the bead being trapped and transported by the robot over a barrier. See Video part 2 for the details.

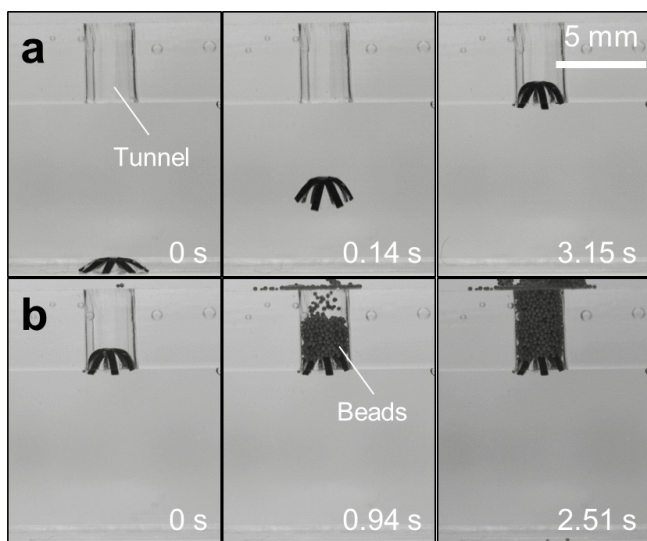


Figure 7. Tube/channel clogging (embolization) demonstration: (a) The robot swims from the tank bottom and docks at the orifice of the tube. (b) The beads pumped from the top are blocked within the tube. See Video part 2 for the details.

Second, we show that the robot can swim into and clog a narrow tube or channel actively. Such clogging is inspired for embolization medical applications, where a blood vessel or the fallopian tube is clogged using different methods due to some vascular aneurysms or to control birth for women, respectively [32], [33]. A cylindrical tube with a diameter of 3 mm is created right above the robot. The robot is controlled to swim from the tank bottom by applying the control signal with the waveform of large amplitude (the red profile in Fig. 4a) at an oscillating frequency of 15 Hz. The robot is then navigated into the tunnel and docks at the orifice. When the magnetic \mathbf{B} field is turned off, the robot can still stay at the orifice due to the friction between the body and the inner wall of the tunnel. To demonstrate the tunnel is indeed blocked, we use a pipette to pump beads from the top of the tunnel. Almost all of the beads are restricted within the tunnel, providing an extra pressure of around 118 Pa on the robot body. The whole blocking process is shown in Fig. 7 and the second scene of the Video part 2.

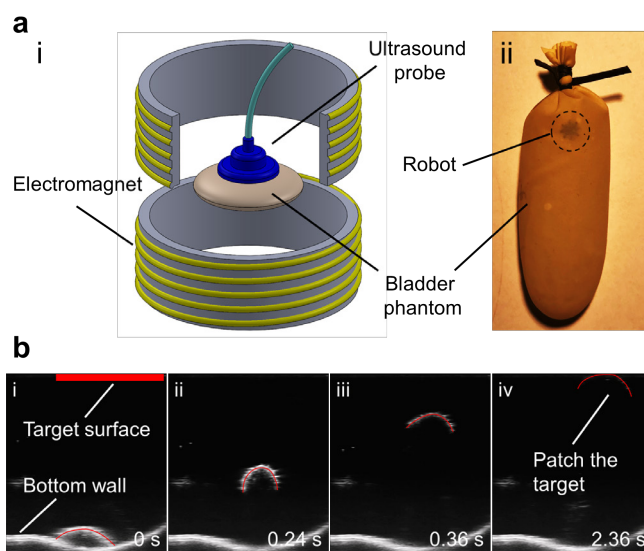


Figure 8. Demonstration of patching a target surface inside a bladder model by the robot, guided by ultrasound imaging: (a) The experiment setup: (i) The coil system; (ii) The bladder phantom. (b) Patching the target surface by the robot while guiding it under ultrasound imaging. The target surface is marked with a red thick line. The robot body is marked with thin red curves. See Video part 2 for the details.

Lastly, we demonstrate the possibility of the robot to patch a target surface mimicking cancerous tissue inside a bladder organ phantom while guiding it under ultrasound imaging. This experiment is motivated by the treatment of the early stage of bladder cancer. Current approaches for treatments include transurethral resection of bladder tumor (TURBT) [34], radiation therapy, and chemotherapy [35]. However, these methods may either cause pain, complications, or irreversible damages to healthy tissues [35], [36]. Our proposed miniature robot as the active patch could deliver chemotherapy drugs locally to the cancer tissue after attaching to reduce any side effects to the patient. This experiment is conducted in a Helmholtz coil system with large working space for inserting the ultrasound probe easily (Fig. 8a-i). To mimic the *in vivo* biological environment of a bladder, a bladder phantom is made

by filling water into a latex balloon (Fig. 8a-ii). The probe of the ultrasound imaging platform (Fujifilm Vevo3100 Imaging System) is inserted from the top of the coil system and pushed onto the surface of the phantom to locate the initial position of the robot (Fig. 8b-i). When applying the control signal of a large amplitude waveform (the red profile in Fig. 4a) at an oscillating frequency of 15 Hz, the robot can immediately swim upwards and finally patches to the upper wall of the phantom (Fig. 8b-iv). The whole process is shown in Fig. 8b and the last scene of the Video part 2. In the future, the drugs can be loaded on the robot body and released directly at the affiliated point. For example, we can replace the non-magnetic soft material with gelatin [37] containing drugs. After the robot patches to the target, the drug can be released slowly and continuously. Moreover, the experiment also shows the position of the robot can be tracked in real-time by ultrasound imaging. Such a technique can provide closed-loop feedback control for future precise positioning of the robot in the future.

VII. CONCLUSION AND FUTURE WORK

A jellyfish-inspired soft millirobot is proposed using magnetic soft composite materials. Its control can be realized by simply tuning the waveform, frequency, and oscillating direction of the external magnetic field. Preliminary investigations have been conducted to find the relationship between its propulsion speed and the input control signal. When the actuation frequency increases, the beating amplitude of the robot monotonically decreases due to the hydrodynamic damping force. Both the experimental data and the modeling prediction suggest the existence of an optimal actuation frequency to a certain control waveform. Preliminary experiments have demonstrated that the robot could realize multiple potential medical functions inside organs filled with a stagnant fluid by delivering cargo (e.g., drug) locally, clogging a narrow tube for embolization, and patching a cancer tissue region or wound under ultrasound imaging. As future works, these functions will be demonstrated in *in vivo* small animal models and the robot's position control will be semi-automated using ultrasound image feedback.

REFERENCES

- [1] M. Sitti, H. Ceylan, W. Hu, J. Giltinan, M. Turan, S. Yim, and E. Diller, "Biomedical Applications of Untethered Mobile Milli/Microrobots," *Proc. IEEE*, vol. 103, pp. 205–224, 2015.
- [2] J. Frame, N. Lopez, O. Curet, and E. D. Engeberg, "Thrust force characterization of free-swimming soft robotic jellyfish," *Bioinspir. Biomim.*, vol. 13, pp. 064001, 2018.
- [3] T. Cheng, G. Li, Y. Liang, M. Zhang, G. Wang, Y. Tao, and T. Li, "Untethered soft robotic jellyfish," *Smart Mater. Struct.*, vol. 1, pp. 102, 2019.
- [4] Y. Chen, H. Wang, E. F. Helbling, N. T. Jafferis, R. Zufferey, A. Ong, K. Ma, N. Gravish, P. Chirarattananon, M. Kovac, and R. J. Wood, "A biologically inspired, flapping-wing, hybrid aerial-aquatic microrobot," *Sci. Robot.*, vol. 2, 2017.
- [5] Z. Wu, J. Troll, H.-H. Jeong, Q. Wei, M. Stang, F. Ziemssen, Z. Wang, M. Dong, S. Schnichels, and T. Qiu, "A swarm of slippery micropropellers penetrates the vitreous body of the eye," *Sci. Adv.*, vol. 4, pp. 1–11, 2018.
- [6] L. Ricotti, B. Trimmer, A. W. Feinberg, R. Raman, K. K. Parker, R. Bashir, M. Sitti, S. Martel, P. Dario, and A. Menciassi, "Biohybrid actuators for robotics: A review of devices actuated by living cells," *Sci. Robot.*, vol. 2, pp. 1–18, 2017.
- [7] L. Hines, K. Petersen, G. Z. Lum, and M. Sitti, "Soft Actuators for Small-Scale Robotics," *Adv. Mater.*, vol. 29, pp. 1603483, 2017.
- [8] M. Sitti, "Voyage of the microrobots Speciation affects ecosystems," *Nature*, vol. 458, pp. 1121–1122, 2009.
- [9] B. J. Nelson, I. K. Kaliakatsos, and J. J. Abbott, "Microrobots for Minimally Invasive Medicine," *Annu. Rev. Biomed. Eng.*, vol. 12, pp. 55–85, 2010.
- [10] M. Sitti, "Miniature soft robots - road to the clinic," *Nat. Rev. Mater.*, vol. 3, pp. 74–75, 2018.
- [11] K. E. Peyer, L. Zhang, and B. J. Nelson, "Bio-inspired magnetic swimming microrobots for biomedical applications," *Nanoscale*, vol. 5, pp. 1259–1272, 2013.
- [12] H. W. Huang, M. S. Sakar, A. J. Petruska, S. Pané, and B. J. Nelson, "Soft micromachines with programmable motility and morphology," *Nat. Commun.*, vol. 7, pp. 1–10, 2016.
- [13] W. Hu, G. Z. Lum, M. Mastrangeli, and M. Sitti, "Small-scale soft-bodied robot with multimodal locomotion," *Nature*, vol. 554, pp. 81–85, 2018.
- [14] T. H. Ware, M. E. McConney, J. J. Wie, V. P. Tondiglia, and T. J. White, "Voxelated liquid crystal elastomers: Supplementary Materials," *Science*, vol. 347, pp. 982–984, 2015.
- [15] C. Christianson, N. N. Goldberg, D. D. Deheyn, S. Cai, and M. T. Tolley, "Translucent soft robots driven by frameless fluid electrode dielectric elastomer actuators," *Sci. Robot.*, vol. 3, pp. eaat1893, 2018.
- [16] S. Maeda, Y. Hara, T. Sakai, R. Yoshida, and S. Hashimoto, "Self-walking gel," *Adv. Mater.*, vol. 19, pp. 3480–3484, 2007.
- [17] N. Kellaris, V. G. Venkata, G. M. Smith, S. K. Mitchell, and C. Keplinger, "Peano-HASEL actuators: Muscle-mimetic, electrohydraulic transducers that linearly contract on activation," *Sci. Robot.*, vol. 3, pp. 1–11, 2018.
- [18] L. Hines, K. Petersen, and M. Sitti, "Inflated Soft Actuators with Reversible Stable Deformations," *Adv. Mater.*, vol. 28, pp. 3690–3696, 2016.
- [19] Z. Wei, Z. Jia, J. Athas, C. Wang, S. R. Raghavan, T. Li, and Z. Nie, "Hybrid hydrogel sheets that undergo pre-programmed shape transformations," *Soft Matter*, vol. 10, pp. 8157–8162, 2014.
- [20] W. Jiang, D. Niu, H. Liu, C. Wang, T. Zhao, L. Yin, Y. Shi, B. Chen, Y. Ding, and B. Lu, "Photoresponsive soft-robotic platform: Biomimetic fabrication and remote actuation," *Adv. Funct. Mater.*, vol. 24, pp. 7598–7604, 2014.
- [21] G. Z. Lum, Z. Ye, X. Dong, H. Marvi, O. Erin, W. Hu, and M. Sitti, "Shape-programmable magnetic soft matter," *Proc. Natl. Acad. Sci.*, vol. 113, pp. E6007–E6015, 2016.
- [22] X. Kim, Yoonho and Yuk, Hyunwoo and Zhao, Ruike and Chester, Shawn A and Zhao, "Printing ferromagnetic domains for untethered fast-transforming soft materials," *Nature*, vol. 558, pp. 274, 2018.
- [23] I. C. Atkinson, L. Renteria, H. Burd, N. H. Pliskin, and K. R. Thulborn, "Safety of human MRI at static fields above the FDA 8T guideline: Sodium imaging at 9.4T does not affect vital signs or cognitive ability," *J. Magn. Reson. Imaging*, vol. 26, pp. 1222–1227, 2007.
- [24] L. A. Zaremba, "Guidance for industry and FDA staff: Criteria for significant risk investigations of magnetic resonance diagnostic devices," *US Dep. Heal. Hum. Serv. Food Drug Adm.*, vol. 14, 2003.
- [25] E. Diller, J. Zhuang, G. Z. Lum, M. R. Edwards, and M. Sitti, "Continuously distributed magnetization profile for millimeter-scale elastomeric undulatory swimming," *Appl. Phys. Lett.*, vol. 104, pp. 174101, 2014.
- [26] H. Lu, M. Zhang, Y. Yang, Q. Huang, T. Fukuda, Z. Wang, and Y. Shen, "A bioinspired multilegged soft millirobot that functions in both dry and wet conditions," *Nat. Commun.*, vol. 9, pp. 3944, 2018.
- [27] J. E. Purcell and D. L. Angel, *Jellyfish Blooms: New Problems and Solutions*, vol. 212, pp. 3–21, 2010.
- [28] B. K. Sullivan, C. L. Suchman, and J. H. Costello, "Mechanics of prey selection by ephyrae of the scyphomedusa *Aurelia aurita*," *Mar. Biol.*, vol. 130, pp. 213–222, 1997.

- [29] T. Blough, S. P. Colin, J. H. Costello, and A. C. Marques, "Ontogenetic Changes in the Bell Morphology and Kinematics and Swimming Behavior of Rowing Medusae: The Special Case of the Limnomedusa *Liriope tetraphylla*," *Biol. Bull.*, vol. 220, pp. 6–14, 2011.
- [30] M. J. McHenry and J. Jed, "The ontogenetic scaling of hydrodynamics and swimming performance in jellyfish (*Aurelia aurita*)," *J. Exp. Biol.*, pp. 4125–4137, 2003.
- [31] R. Turton, "A Short Note on the Drag Correlation for Spheres," *Powder Technol.*, vol. 47, pp. 83–86, 1986.
- [32] I. H. Foundation, "Women's Satisfaction with Birth Control: A Population Survey," *Contraception*, vol. 59, pp. 277–86, 1999.
- [33] D. C. Brewster, J. L. Cronenwett, J. W. Hallett, K. W. Johnston, W. C. Krupski, and J. S. Matsumura, "Guidelines for the treatment of abdominal aortic aneurysms: Report of a subcommittee of the Joint Council of the American Association for Vascular Surgery and Society for Vascular Surgery," *J. Vasc. Surg.*, vol. 37, pp. 1106–1117, 2003.
- [34] M. Richterstetter, B. Wullich, K. Amann, L. Haeberle, D. G. Engehausen, P. J. Goebell, and F. S. Krause, "The value of extended transurethral resection of bladder tumour (TURBT) in the treatment of bladder cancer," *BJU Int.*, vol. 110, pp. 76–79, 2012.
- [35] J. P. Stein, G. Lieskovsky, R. Cote, S. Groshen, A. C. Feng, S. Boyd, E. Skinner, B. Bochner, D. Thangathurai, M. Mikhail, D. Raghavan, and D. G. Skinner, "Radical cystectomy in the treatment of invasive bladder cancer: Long-term results in 1,054 patients," *J. Clin. Oncol.*, vol. 19, pp. 666–675, 2001.
- [36] O. Traxer, F. Pasqui, B. Gattegno, and M. S. Pearle, "Technique and complications of transurethral surgery for bladder tumours," *BJU Int.*, vol. 94, pp. 492–496, 2004.
- [37] H. Ceylan, I. C. Yasa, O. Yasa, A. F. Tabak, J. Giltinan, and M. Sitti, "3D-Printed Biodegradable Microswimmer for Theranostic Cargo Delivery," *ACS Nano*, vol. 13, pp. 3353–3362, 2019.